The exposure of the hybrid detector of the Pierre Auger Observatory

The Pierre Auger Collaboration

P. Abreu[73], M. Aglietta[55], E.J. Ahn[89], D. Allard[31], I. Allekotte[1], J. Allen[92], J. Alvarez Castillo[66], J. Alvarez-Muñiz[80], M. Ambrosio[48], A. Aminaei[67], L. Anchordoqui[106], S. Andringa[73], T. Antičić[25], A. Anzalone[54], C. Aramo[48], E. Arganda[77], K. Arisaka[97], F. Arqueros[77], H. Asorey[1], P. Assis[73], J. Aublin[33], M. Ave[37, 98], M. Avenier[34], G. Avila[10], T. Bäcker[43], D. Badagnani[6], M. Balzer[38], K.B. Barber[11], A.F. Barbosa[14], R. Bardenet[32], S.L.C. Barroso[20], B. Baughman[94], J.J. Beatty[94], B.R. Becker[103], K.H. Becker[36], A. Bellétoile[34], J.A. Bellido[11], S. BenZvi[105], C. Berat[34], T. Bergmann[38], X. Bertou[1], P.L. Biermann[40], P. Billoir[33], F. Blanco[77], M. Blanco[78], C. Bleve[36, 47], H. Blümer[39, 37], M. Boháčová[98, 27], D. Boncioli[49], C. Bonifazi[23, 33], R. Bonino[55], N. Borodai[71], J. Brack[87], P. Brogueira[73], W.C. Brown[88], R. Bruijn[83], P. Buchholz[43], A. Bueno[79], R.E. Burton[85], N.G. Busca[31], K.S. Caballero-Mora[39], L. Caramete[40], R. Caruso[50], A. Castellina[55], O. Catalano[54], G. Cataldi[47], L. Cazon[73], R. Cester[51], J. Chauvin[34], A. Chiavassa[55], J.A. Chinellato[18], A. Chou[89, 92], J. Chudoba[27], R.W. Clay[11], E. Colombo[2], M.R. Coluccia[47], R. Conceição[73], F. Contreras[9], H. Cook[83], M.J. Cooper[11], J. Coppens[67, 69], A. Cordier[32], U. Cotti[65], S. Coutu[95], C.E. Covault[85], A. Creusot[75], A. Criss[95], J. Cronin[98], A. Curutiu[40], S. Dagoret-Campagne[32], R. Dallier[35], S. Dasso[7, 4], K. Daumiller[37], B.R. Dawson[11], R.M. de Almeida[18, 23], M. De Domenico[50], C. De Donato[66, 46], S.J. de Jong[67], G. De La Vega[8], W.J.M. de Mello Junior[18], J.R.T. de Mello Neto[23], I. De Mitri[47], V. de Souza[16], K.D. de Vries[68], G. Decerprit[31], L. del Peral[78], O. Deligny[30], A. Della Selva[48], H. Dembinski[37], A. Denkiewicz[2], C. Di Giulio[49], J.C. Diaz[91], M.L. Díaz Castro[15], P.N. Diep[107], C. Dobrigkeit [18], J.C. D'Olivo[66], P.N. Dong[107, 30], A. Dorofeev[87], J.C. dos Anjos[14], M.T. Dova[6], D. D'Urso[48], I. Dutan[40], J. Ebr[27], R. Engel[37], M. Erdmann[41], C.O. Escobar[18], A. Etchegoyen[2], P. Facal San Luis[98], H. Falcke[67, 70], G. Farrar[92], A.C. Fauth[18], N. Fazzini[89], A.P. Ferguson[85], A. Ferrero[2], B. Fick[91], A. Filevich[2], A. Filipčič[74, 75], I. Fleck[43], S. Fliescher[41], C.E. Fracchiolla[87], E.D. Fraenkel[68], U. Fröhlich[43], B. Fuchs[14], W. Fulgione[55], R.F. Gamarra[2], S. Gambetta[44], B. García[8], D. García Gámez[79], D. Garcia-Pinto[77], X. Garrido[37], A. Gascon[79], G. Gelmini[97], H. Gemmeke[38], K. Gesterling[103], P.L. Ghia[30, 55], U. Giaccari[47], M. Giller[72], H. Glass[89], M.S. Gold[103], G. Golup[1], F. Gomez Albarracin[6], M. Gómez Berisso[1], P. Gonçalves[73], D. Gonzalez[39], J.G. Gonzalez[39], B. Gookin[87], D. Góra[39, 71], A. Gorgi[55], P. Gouffon[17], S.R. Gozzini[83], E. Grashorn[94], S. Grebe[67], M. Grigat[41], A.F. Grillo[56], Y. Guardincerri[4],

1 November 2010

F. Guarino[48], G.P. Guedes[19], J.D. Hague[103], P. Hansen[6], D. Harari[1], S. Harmsma[68, 69], J.L. Harton[87], A. Haungs[37], T. Hebbeker[41], D. Heck[37], A.E. Herve[11], C. Hojvat[89], V.C. Holmes[11], P. Homola[71], J.R. Hörandel[67], A. Horneffer[67], M. Hrabovský[28, 27], T. Huege[37], A. Insolia[50], F. Ionita[98], A. Italiano[50], S. Jiraskova[67], K. Kadija[25], M. Kaducak[89], K.H. Kampert[36], P. Karhan[26], T. Karova[27], P. Kasper[89], B. Kégl[32], B. Keilhauer[37], A. Keivani[90], J.L. Kelley[67], E. Kemp[18], R.M. Kieckhafer[91], H.O. Klages[37], M. Kleifges[38], J. Kleinfeller[37], J. Knapp[83], D.-H. Koang[34], K. Kotera[98], N. Krohm[36], O. Krömer[38], D. Kruppke-Hansen[36], F. Kuehn[89], D. Kuempel[36], J.K. Kulbartz[42], N. Kunka[38], G. La Rosa[54], C. Lachaud[31], P. Lautridou[35], M.S.A.B. Leão[22], D. Lebrun[34], P. Lebrun[89], M.A. Leigui de Oliveira[22], A. Lemiere[30], A. Letessier-Selvon[33], I. Lhenry-Yvon[30], K. Link[39], R. López[61], A. Lopez Agüera[80], K. Louedec[32], J. Lozano Bahilo[79], A. Lucero[2, 55], M. Ludwig[39], H. Lyberis[30], M.C. Maccarone[54], C. Macolino[33, 45], S. Maldera[55], D. Mandat[27], P. Mantsch[89], A.G. Mariazzi[6], V. Marin[35], I.C. Maris[33], H.R. Marquez Falcon[65], G. Marsella[52], D. Martello[47], L. Martin[35], O. Martínez Bravo[61], H.J. Mathes[37], J. Matthews[90, 96], J.A.J. Matthews[103], G. Matthiae[49], D. Maurizio[51], P.O. Mazur[89], M. McEwen[78], G. Medina-Tanco[66], M. Melissas[39], D. Melo[51], E. Menichetti[51], A. Menshikov[38], C. Meurer[41], S. Mičanović[25], M.I. Micheletti[2], W. Miller[103], L. Miramonti[46], S. Mollerach[1], M. Monasor[98], D. Monnier Ragaigne[32], F. Montanet[34], B. Morales[66], C. Morello[55], E. Moreno[61], J.C. Moreno[6], C. Morris[94], M. Mostafá[87], S. Mueller[37], M.A. Muller[18], M. Münchmeyer[33], R. Mussa[51], G. Navarra[55 †], J.L. Navarro[79], S. Navas[79], P. Necesal[27], L. Nellen[66], P.T. Nhung[107], N. Nierstenhoefer[36], D. Nitz[91], D. Nosek[26], L. Nožka[27], M. Nyklicek[27], J. Oehlschläger[37], A. Olinto[98], P. Oliva[36], V.M. Olmos-Gilbaja[80], M. Ortiz[77], N. Pacheco[78], D. Pakk Selmi-Dei[18], M. Palatka[27], J. Pallotta[3], N. Palmieri[39], G. Parente[80], E. Parizot[31], A. Parra[80], J. Parrisius[39], R.D. Parsons[83], S. Pastor[76], T. Paul[93], V. Pavlidou[98 c], K. Payet[34], M. Pech[27], J. Pękala[71], R. Pelayo[80], I.M. Pepe[21], L. Perrone[52], R. Pesce[44], E. Petermann[102], S. Petrera[45], P. Petrinca[49], A. Petrolini[44], Y. Petrov[87], J. Petrovic[69], C. Pfendner[105], N. Phan[103], R. Piegaia[4], T. Pierog[37], M. Pimenta[73], V. Pirronello[50], M. Platino[2], V.H. Ponce[1], M. Pontz[43], P. Privitera[98], M. Prouza[27], E.J. Quel[3], J. Rautenberg[36], O. Ravel[35], D. Ravignani[2], B. Revenu[35], J. Ridky[27], S. Riggi[50], M. Risse[43], P. Ristori[3], H. Rivera[46], C. Rivière[34], V. Rizi[45], C. Robledo[61], G. Rodriguez[80], J. Rodriguez Martino[9, 50], J. Rodriguez Rojo[9], I. Rodriguez-Cabo[80], M.D. Rodríguez-Frías[78], G. Ros[78], J. Rosado[77], T. Rossler[28], M. Roth[37], B. Rouillé-d'Orfeuil[98], E. Roulet[1], A.C. Rovero[7], F. Salamida[37, 45], H. Salazar[61], G. Salina[49], F. Sánchez[2], M. Santander[9], C.E. Santo[73], E. Santos[73], E.M. Santos[23], F. Sarazin[86], S. Sarkar[81], R. Sato[9], N. Scharf[41], V. Scherini[46], H. Schieler[37], P. Schiffer[41], A. Schmidt[38], F. Schmidt[98], T. Schmidt[39], O. Scholten[68], H. Schoorlemmer[67], J. Schovancova[27], P. Schovánek[27], F. Schroeder[37], S. Schulte[41],

F. Schüssler[37], D. Schuster[86], S.J. Sciutto[6], M. Scuderi[50], A. Segreto[54], D. Semikoz[31], M. Settimo[47], A. Shadkam[90], R.C. Shellard[14, 15], I. Sidelnik[2], G. Sigl[42], A. Śmiałkowski[72], R. Šmída[37, 27], G.R. Snow[102], P. Sommers[95], J. Sorokin[11], H. Spinka[84, 89], R. Squartini[9], J. Stapleton[94], J. Stasielak[71], M. Stephan[41], E. Strazzeri[54], A. Stutz[34], F. Suarez[2], T. Suomijärvi[30], A.D. Supanitsky[66], T. Šuša[25], M.S. Sutherland[94], J. Swain[93], Z. Szadkowski[36, 72], A. Tamashiro[7], A. Tapia[2], T. Tarutina[6], O. Taşcău[36], R. Tcaciuc[43], D. Tcherniakhovski[38], D. Tegolo[50, 59], N.T. Thao[107], D. Thomas[87], J. Tiffenberg[4], C. Timmermans[69, 67], D.K. Tiwari[65], W. Tkaczyk[72], C.J. Todero Peixoto[22], B. Tomé[73], A. Tonachini[51], P. Travnicek[27], D.B. Tridapalli[17], G. Tristram[31], E. Trovato[50], M. Tueros[6], R. Ulrich[95, 37], M. Unger[37], M. Urban[32], J.F. Valdés Galicia[66], I. Valiño[37], L. Valore[48], A.M. van den Berg[68], B. Vargas Cárdenas[66], J.R. Vázquez[77], R.A. Vázquez[80], D. Veberič[75, 74], T. Venters[98], V. Verzi[49], M. Videla[8], L. Villaseñor[65], H. Wahlberg[6], P. Wahrlich[11], O. Wainberg[2], D. Warner[87], A.A. Watson[83], K. Weidenhaupt[41], A. Weindl[37], S. Westerhoff[105], B.J. Whelan[11], G. Wieczorek[72], L. Wiencke[86], B. Wilczyńska[71], H. Wilczyński[71], M. Will[37], C. Williams[98], T. Winchen[41], L. Winders[106], M.G. Winnick[11], M. Wommer[37], B. Wundheiler[2], T. Yamamoto[98 a], P. Younk[87], G. Yuan[90], A. Yushkov[48], B. Zamorano[79], E. Zas[80], D. Zavrtanik[75, 74], M. Zavrtanik[74, 75], I. Zaw[92], A. Zepeda[62], M. Ziolkowski[43]

[1] Centro Atómico Bariloche and Instituto Balseiro (CNEA-UNCuyo-CONICET), San Carlos de Bariloche, Argentina
[2] Centro Atómico Constituyentes (Comisión Nacional de Energía Atómica/CONICET/UTN-FRBA), Buenos Aires, Argentina
[3] Centro de Investigaciones en Láseres y Aplicaciones, CITEFA and CONICET, Argentina
[4] Departamento de Física, FCEyN, Universidad de Buenos Aires y CONICET, Argentina
[6] IFLP, Universidad Nacional de La Plata and CONICET, La Plata, Argentina
[7] Instituto de Astronomía y Física del Espacio (CONICET- UBA), Buenos Aires, Argentina
[8] National Technological University, Faculty Mendoza (CONICET/CNEA), Mendoza, Argentina
[9] Pierre Auger Southern Observatory, Malargüe, Argentina
[10] Pierre Auger Southern Observatory and Comisión Nacional de Energía Atómica, Malargüe, Argentina
[11] University of Adelaide, Adelaide, S.A., Australia
[14] Centro Brasileiro de Pesquisas Fisicas, Rio de Janeiro, RJ, Brazil
[15] Pontifícia Universidade Católica, Rio de Janeiro, RJ, Brazil
[16] Universidade de São Paulo, Instituto de Física, São Carlos, SP, Brazil
[17] Universidade de São Paulo, Instituto de Física, São Paulo, SP, Brazil
[18] Universidade Estadual de Campinas, IFGW, Campinas, SP, Brazil

[19] Universidade Estadual de Feira de Santana, Brazil
[20] Universidade Estadual do Sudoeste da Bahia, Vitoria da Conquista, BA, Brazil
[21] Universidade Federal da Bahia, Salvador, BA, Brazil
[22] Universidade Federal do ABC, Santo André, SP, Brazil
[23] Universidade Federal do Rio de Janeiro, Instituto de Física, Rio de Janeiro, RJ, Brazil
[25] Rudjer Bošković Institute, 10000 Zagreb, Croatia
[26] Charles University, Faculty of Mathematics and Physics, Institute of Particle and Nuclear Physics, Prague, Czech Republic
[27] Institute of Physics of the Academy of Sciences of the Czech Republic, Prague, Czech Republic
[28] Palacký University, Olomouc, Czech Republic
[30] Institut de Physique Nucléaire d'Orsay (IPNO), Université Paris 11, CNRS-IN2P3, Orsay, France
[31] Laboratoire AstroParticule et Cosmologie (APC), Université Paris 7, CNRS-IN2P3, Paris, France
[32] Laboratoire de l'Accélérateur Linéaire (LAL), Université Paris 11, CNRS-IN2P3, Orsay, France
[33] Laboratoire de Physique Nucléaire et de Hautes Energies (LPNHE), Universités Paris 6 et Paris 7, CNRS-IN2P3, Paris, France
[34] Laboratoire de Physique Subatomique et de Cosmologie (LPSC), Université Joseph Fourier, INPG, CNRS-IN2P3, Grenoble, France
[35] SUBATECH, CNRS-IN2P3, Nantes, France
[36] Bergische Universität Wuppertal, Wuppertal, Germany
[37] Karlsruhe Institute of Technology - Campus North - Institut für Kernphysik, Karlsruhe, Germany
[38] Karlsruhe Institute of Technology - Campus North - Institut für Prozessdatenverarbeitung und Elektronik, Karlsruhe, Germany
[39] Karlsruhe Institute of Technology - Campus South - Institut für Experimentelle Kernphysik (IEKP), Karlsruhe, Germany
[40] Max-Planck-Institut für Radioastronomie, Bonn, Germany
[41] RWTH Aachen University, III. Physikalisches Institut A, Aachen, Germany
[42] Universität Hamburg, Hamburg, Germany
[43] Universität Siegen, Siegen, Germany
[44] Dipartimento di Fisica dell'Università and INFN, Genova, Italy
[45] Università dell'Aquila and INFN, L'Aquila, Italy
[46] Università di Milano and Sezione INFN, Milan, Italy
[47] Dipartimento di Fisica dell'Università del Salento and Sezione INFN, Lecce, Italy
[48] Università di Napoli "Federico II" and Sezione INFN, Napoli, Italy
[49] Università di Roma II "Tor Vergata" and Sezione INFN, Roma, Italy
[50] Università di Catania and Sezione INFN, Catania, Italy

[51] Università di Torino and Sezione INFN, Torino, Italy
[52] Dipartimento di Ingegneria dell'Innovazione dell'Università del Salento and Sezione INFN, Lecce, Italy
[54] Istituto di Astrofisica Spaziale e Fisica Cosmica di Palermo (INAF), Palermo, Italy
[55] Istituto di Fisica dello Spazio Interplanetario (INAF), Università di Torino and Sezione INFN, Torino, Italy
[56] INFN, Laboratori Nazionali del Gran Sasso, Assergi (L'Aquila), Italy
[59] Università di Palermo and Sezione INFN, Catania, Italy
[61] Benemérita Universidad Autónoma de Puebla, Puebla, Mexico
[62] Centro de Investigación y de Estudios Avanzados del IPN (CINVESTAV), México, D.F., Mexico
[65] Universidad Michoacana de San Nicolas de Hidalgo, Morelia, Michoacan, Mexico
[66] Universidad Nacional Autonoma de Mexico, Mexico, D.F., Mexico
[67] IMAPP, Radboud University, Nijmegen, Netherlands
[68] Kernfysisch Versneller Instituut, University of Groningen, Groningen, Netherlands
[69] NIKHEF, Amsterdam, Netherlands
[70] ASTRON, Dwingeloo, Netherlands
[71] Institute of Nuclear Physics PAN, Krakow, Poland
[72] University of Łódź, Łódź, Poland
[73] LIP and Instituto Superior Técnico, Lisboa, Portugal
[74] J. Stefan Institute, Ljubljana, Slovenia
[75] Laboratory for Astroparticle Physics, University of Nova Gorica, Slovenia
[76] Instituto de Física Corpuscular, CSIC-Universitat de València, Valencia, Spain
[77] Universidad Complutense de Madrid, Madrid, Spain
[78] Universidad de Alcalá, Alcalá de Henares (Madrid), Spain
[79] Universidad de Granada & C.A.F.P.E., Granada, Spain
[80] Universidad de Santiago de Compostela, Spain
[81] Rudolf Peierls Centre for Theoretical Physics, University of Oxford, Oxford, United Kingdom
[83] School of Physics and Astronomy, University of Leeds, United Kingdom
[84] Argonne National Laboratory, Argonne, IL, USA
[85] Case Western Reserve University, Cleveland, OH, USA
[86] Colorado School of Mines, Golden, CO, USA
[87] Colorado State University, Fort Collins, CO, USA
[88] Colorado State University, Pueblo, CO, USA
[89] Fermilab, Batavia, IL, USA
[90] Louisiana State University, Baton Rouge, LA, USA
[91] Michigan Technological University, Houghton, MI, USA
[92] New York University, New York, NY, USA
[93] Northeastern University, Boston, MA, USA

[94] Ohio State University, Columbus, OH, USA
[95] Pennsylvania State University, University Park, PA, USA
[96] Southern University, Baton Rouge, LA, USA
[97] University of California, Los Angeles, CA, USA
[98] University of Chicago, Enrico Fermi Institute, Chicago, IL, USA
[102] University of Nebraska, Lincoln, NE, USA
[103] University of New Mexico, Albuquerque, NM, USA
[105] University of Wisconsin, Madison, WI, USA
[106] University of Wisconsin, Milwaukee, WI, USA
[107] Institute for Nuclear Science and Technology (INST), Hanoi, Vietnam
(†) Deceased
(a) at Konan University, Kobe, Japan
(c) at Caltech, Pasadena, USA

Abstract

The Pierre Auger Observatory is a detector for ultra-high energy cosmic rays. It consists of a surface array to measure secondary particles at ground level and a fluorescence detector to measure the development of air showers in the atmosphere above the array. The "hybrid" detection mode combines the information from the two subsystems. We describe the determination of the hybrid exposure for events observed by the fluorescence telescopes in coincidence with at least one water-Cherenkov detector of the surface array. A detailed knowledge of the time dependence of the detection operations is crucial for an accurate evaluation of the exposure. We discuss the relevance of monitoring data collected during operations, such as the status of the fluorescence detector, background light and atmospheric conditions, that are used in both simulation and reconstruction.

Key words: Ultra high energy cosmic rays, Pierre Auger Observatory, Extensive air showers, Trigger, Exposure, Fluorescence detector, Hybrid

1 Introduction

The Pierre Auger Observatory has been designed to investigate the origin and the nature of Ultra High Energy Cosmic Rays. It consists of a large array of about 1600 surface stations (the *SD array*) covering an area of 3000 km^2 for detecting the secondary particles of the air shower at ground level by means of the Cherenkov radiation they produce in water. The ground array is overlooked by 24 air fluorescence telescopes (the *FD system*), grouped in 4 enclosures each consisting of 6 optical telescopes. These devices are used to observe the longitudinal profile of cosmic ray showers on clear moonless nights. The Observatory, located outside the town of Malargüe, in the Province

of Mendoza, Argentina, has been taking data stably since January 2004 while the construction was proceeding. The construction was completed in mid 2008. Details of the design, construction and performance of the Observatory can be found in [1,2,3].

The Auger detector has been conceived with a cross-triggering capability. Data are retrieved from both detectors whenever either system is triggered [1] . The surface array and the fluorescence telescopes allow the reconstruction of extensive air showers with two independent measurements. The combination of information from the two detection subsystems enhances the reconstruction capability with respect to the individual detector components [5,6]. This technique is called "hybrid" detection and the determination of the exposure of the Observatory under this mode is the subject of the present paper. The data period used for this purpose is between November 2005 and May 2008. The exposure calculated here is the same used for the energy spectrum measurement published in ([7]).

The paper is organized as follows. In section 2 we describe the hybrid detection method. Section 3 addresses the energy spectrum and the relevance of the hybrid exposure to its determination. The effective data taking time in the hybrid detection mode, i.e the hybrid on-time, and the different components contributing to it are discussed in section 4. The Monte Carlo simulation used for the evaluation of the hybrid exposure is described in section 5. In section 6 we describe the event selection and make comparisons with data to validate the Monte Carlo simulation. Finally in section 7 we show the hybrid exposure as a function of primary energy and in section 8 we summarize.

2 Hybrid data analysis

A *hybrid* event is an air shower that is simultaneously detected by the fluorescence detector and the surface array. If an air shower independently triggers both detectors the event is tagged as a *golden hybrid* and these events can be fully reconstructed in both detection modes. In the SD the energy density of shower particles at ground level is used to determine the cosmic ray energy. In the FD the observation of the longitudinal profile of the shower allows the measurement of the calorimetric energy of the primary particle. This event sample, though small with respect to the SD sample, is very important since it constitutes the base data set for the energy calibration of the SD events [8,6].

[1] Details about the triggers implemented can be found in [4] for the SD and in [3] for the FD.

The fluorescence detector, having a lower energy threshold, may promote a sub-threshold trigger in the SD. In this case, surface stations are matched by timing and location even though they do not fulfil the conditions for an independent SD trigger. This is an important capability because these sub-threshold *hybrid* events would not have triggered the array otherwise. Here the energy reconstruction relies uniquely on the calorimetric energy from the longitudinal profile.

Like *golden hybrids* these events suffer statistical limitations, but they are of particular interest because they allow an extension of the measurement of the energy spectrum into a region where the SD is not fully efficient [4]. They have superior qualities with respect to "monocular" FD events (those without SD information), because of the precise measurement of the shower geometry [3].

In the FD, cosmic ray showers are detected as a sequence of triggered pixels in a matrix of photomultipliers. This sequence allows the determination of the shower-detector plane (SDP), the plane that includes the location of the fluorescence detector and the line of the shower axis, with a typical uncertainty of the order of a few tenths of a degree. Then the determination of the shower geometry relies on the arrival times of photons in the individual pixels [3]. In the monocular reconstruction the accuracy degrades when the measured angular speed does not change significantly over the observed track length. In such cases the shower axis can be largely under-determined within the SDP, thus giving large uncertainties in the reconstruction of the arrival direction and the impact point at ground level. This further leads to uncertainties in other shower parameters and in particular in the reconstructed shower energy.

The hybrid approach supplements the traditional FD direction fitting method with the arrival time of the shower at the ground measured by a single SD station. This results in a remarkable improvement in the determination of the shower geometry, as illustrated in figure 1 where the impact points at ground level corresponding to mono and hybrid reconstruction methods are shown for a typical event. Accurate knowledge of the shower arrival time at ground level removes a degeneracy in the traditional FD monocular approach that uses pixel timing to reconstruct the shower axis. In hybrid mode, the resolution of the direction and of the position of the impact point at the ground are better than 0.6° and 50 m respectively [9,10,5].

The total energy of each event is obtained by combining the knowledge of the detector response with monitoring data describing the atmospheric conditions [3]. Once the geometry is known, the observed energy deposit profile is reconstructed taking into account the scattering and the absorption of light during its propagation in the atmosphere and the presence of forward-emitted and scattered Cherenkov light. The method used is described in detail in [11]. The energy released in the electromagnetic part of the air shower is estimated

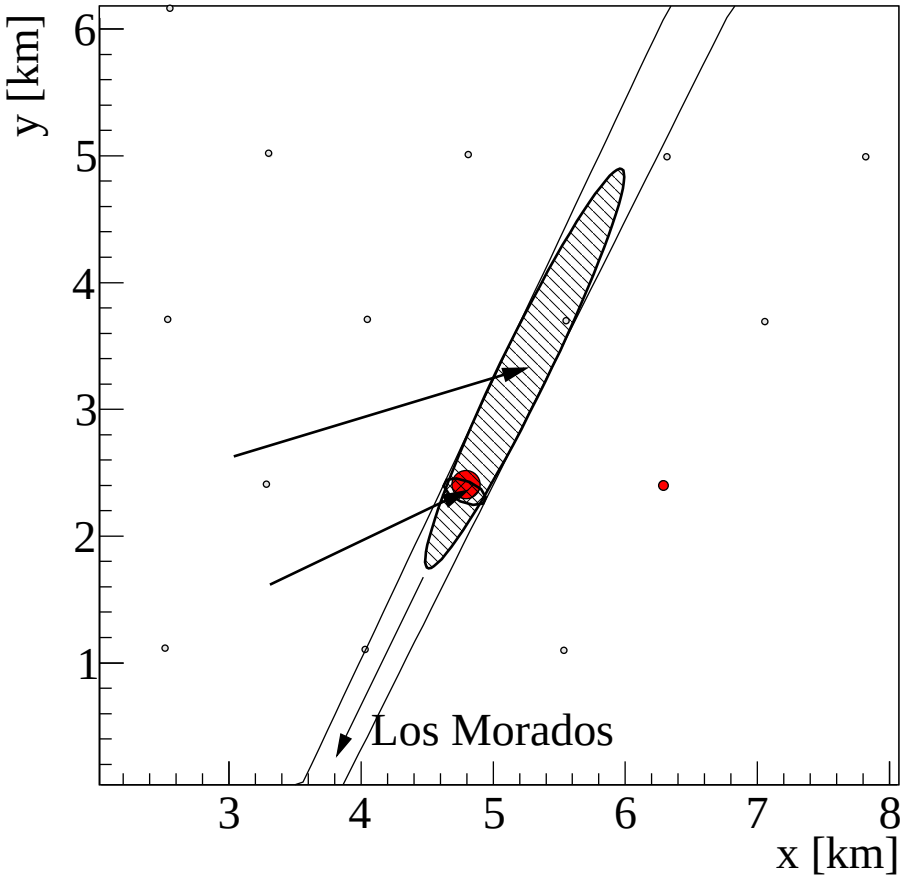

Fig. 1. Determination of the impact point at the ground for a single event using both the mono and hybrid reconstruction methods. The event has been detected by the Los Morados FD site: the downward-going arrow points towards the direction of the site and the two lines show the uncertainty of the SDP plane at ground level. The small (long) elongated ellipse represents the uncertainty on the core position in the hybrid (mono) reconstruction. The arrows indicate the reconstructed directions in the two cases, their length being proportional to the sine of the reconstructed zenith angle. The open (full) circles show the active (triggered) SD stations. Triggered stations are shown with a radius proportional to the logarithm of the signal.

by fitting a Gaisser-Hillas function [12] to the reconstructed energy deposit profile and integrating it over the entire range of atmospheric depth. Finally, the total energy of a shower is derived after correcting for the invisible energy carried away by neutrinos and high energy muons [13]. After quality selection, the energy resolution (defined as an event-to-event statistical uncertainty) of the fluorescence detector is better than 10% [5]. This value has been calculated from simulations and has been cross checked with hybrid-stereo events, i.e. those events which are detected and reconstructed in hybrid mode by more than one FD-site[3]. The energy resolution turned out to be energy independent in the whole range.

Table 1
Current estimates of the systematic uncertainties affecting energy reconstruction. Values from [6].

	uncertainty %		uncertainty %
fluorescence yield (FY)	14	quenching effect on FY	5
FD absolute calibration	9	FD wavelength response	3
molecular attenuation	1	aerosol attenuation	7
multiple scattering model	1	FD reconstruction method	10
invisible energy	4		
total			**22**

Systematic uncertainties in the energy determination are related to the detector, to the atmosphere and to the reconstruction procedure. They are summarized in Tab. 1. All these uncertainties are found to be independent. A total uncertainty of about 22% [6] is estimated by summing the individual contributions in quadrature.

3 Energy Spectrum with hybrid events

The aperture of a cosmic ray instrument is per se a figure of merit of its observation capability. The time integrated aperture is commonly referred to as the exposure. In this section we discuss the relevance of the exposure for the energy spectrum measurement. This is of particular concern in the case of a detection based on fluorescence, such as the hybrid case, where the time variations of the detection and the inherent energy dependence make an accurate determination of the exposure a key task.

The flux of cosmic rays J as a function of energy is defined as:

$$J(E) = \frac{\mathrm{d}^4 N_{\mathrm{inc}}}{\mathrm{d}E \mathrm{d}A \mathrm{d}\Omega \mathrm{d}t} \simeq \frac{\Delta N_{\mathrm{sel}}(E)}{\Delta E} \frac{1}{\mathcal{E}(E)}; \qquad (1)$$

where N_{inc} is the number of cosmic rays with energy between E and $E+\mathrm{d}E$ incident on a surface element $\mathrm{d}A$, within a solid angle $\mathrm{d}\Omega$ and time $\mathrm{d}t$. $\Delta N_{\mathrm{sel}}(E)$ is the number of detected events passing the selection criteria in the energy bin centered around E, having width ΔE. $\mathcal{E}(E)$ represents the energy-dependent exposure of the detector at the same selection level.

The exposure, as a function of the energy of primary particle, can be written as:

$$\mathcal{E}(E) = \int_T \int_\Omega \int_{S_{gen}} \varepsilon(E, t, \theta, \phi, x, y)\ \cos\theta\ \mathrm{d}S\ \mathrm{d}\Omega\ \mathrm{d}t = \int_T \mathcal{A}(E, t)\ \mathrm{d}t; \qquad (2)$$

where ε is the detection efficiency including the different steps of the analysis, i.e trigger, reconstruction and quality cuts, and $\mathrm{d}S = \mathrm{d}x \times \mathrm{d}y$ is the horizontal surface element. $\mathrm{d}\Omega = \sin\theta \mathrm{d}\theta\mathrm{d}\phi$ and Ω are respectively the differential and total solid angles. The generation area $\mathrm{S_{gen}}$ has been chosen large enough to exclude any possible event detection and reconstruction outside it. $\mathcal{A}(E,t)$ is the instantaneous aperture of the detector which depends on the detector configuration at the time t.

The detector configurations of the Observatory have been continuously changing over the period of data collection for the hybrid spectrum. As construction of the SD progressed, the number of stations in operation increased. Furthermore, even in a steady configuration, some SD stations are temporarily out of service at any one time. The SD status is monitored by updating each second the list of "active" stations. In principle the change in SD configuration is straightforward to handle since the aperture is proportional to a geometric area. In the case of a single missing SD station, the effective area is slightly changed by about $2\,\mathrm{km}^2$ at full efficiency [4].

The FD detector configuration also changed with time during the construction phase, with the number of telescopes changing from 12 to 24. In addition, a correction ring lens was added to each telescope during the first two years of data taking. Thus, parts of the data have been collected with different optical configurations. During nightly operations individual telescopes are sometimes deactivated because of increasing sky brightness, bad weather conditions or hardware failures. Finally, the FD response is influenced by atmospheric conditions such as the concentration of aerosols and cloud coverage.

To properly take into account all the detector configurations and their time variability a sample of events which reproduce the exact conditions of the experiment (i.e its actual sequence of configurations and on-time) has been simulated. This method, referred to as *Time Dependent Detector Simulation*, is described in the next sections. Given a set of N simulated events generated on an area $\mathrm{S_{gen}}$ within the time interval T, the exposure eq. (2) can be calculated numerically via

$$\mathcal{E}(E_{\mathrm{rec}}) = 2\pi\ \mathrm{S_{gen}}\ \mathrm{T}\ \sum_i \frac{n(E_{\mathrm{rec}}, \cos\theta_i)}{N(E_{\mathrm{gen}}, \cos\theta_i)}\ \cos\theta_i\ \Delta\cos\theta_i; \tag{3}$$

where n denotes the number of events that fulfill the selection criteria described in Sec. 6. The exposure is calculated as a function of reconstructed energy, E_{rec}, to correct for distortions of the steep energy spectrum due to the finite resolution of the energy reconstruction (see e.g. [14,15] and Sec. 6.3).

4 Hybrid on-time

The efficiency of fluorescence and hybrid data taking is influenced by many effects. These can be external, e.g. lightning or storms, or internal to the data taking itself, e.g. DAQ failures. For the determination of the *on-time* of the Pierre Auger Observatory in the hybrid detection mode it is therefore crucial to take into account all these occurrences and derive a solid description of the data taking time sequence.

Data losses and inefficiencies can occur on different levels, from the smallest unit of the FD, i.e. one single photomultiplier (pixel) readout channel, up to the highest level, i.e. the combined SD-FD data taking of the Observatory. To perform the time dependent detector simulation we have to take into account all known disturbances and then derive the on-time of the hybrid detection mode. To achieve this aim we rely on a variety of monitoring information and the data set itself. As a compromise between accuracy and stability we derived the complete detector status down to the single pixel for time intervals $T_{\mathrm{bin}} = 10$ min.

4.1 Telescope dependent sources

The active time of FD data acquisition is calculated using a minimum bias data stream with a less restrictive trigger condition. This data file includes sub-threshold FD events and is recorded at an event rate about 8 times higher than the standard rate of about 1 event per FD-site per minute.

Even if the DAQ is running, the shutters of the telescope might be closed due to bad weather alarms from the slow control system or other failsafe mechanisms. To determine the status of the shutters we use the information on night sky background level provided by algorithms implemented in the front-end electronics boards. Every 30 s data from each PMT channel is written to a monitoring data file which records parameters including ADC-variance, baseline, First Level Trigger (FLT) threshold and trigger frequency for each pixel [3].

The ADC-variance distribution from these data is shown in figure 2. Background data is also collected during the nightly relative calibration runs, i.e. with closed shutters (see the upper-right panel in figure 2). A mean value of about 3.5 ADC^2 is obtained in these conditions [2]. For each time interval the efficiency of open shutters is then derived as:

[2] Muons hitting the pixel camera is the main source of the noise triggers.

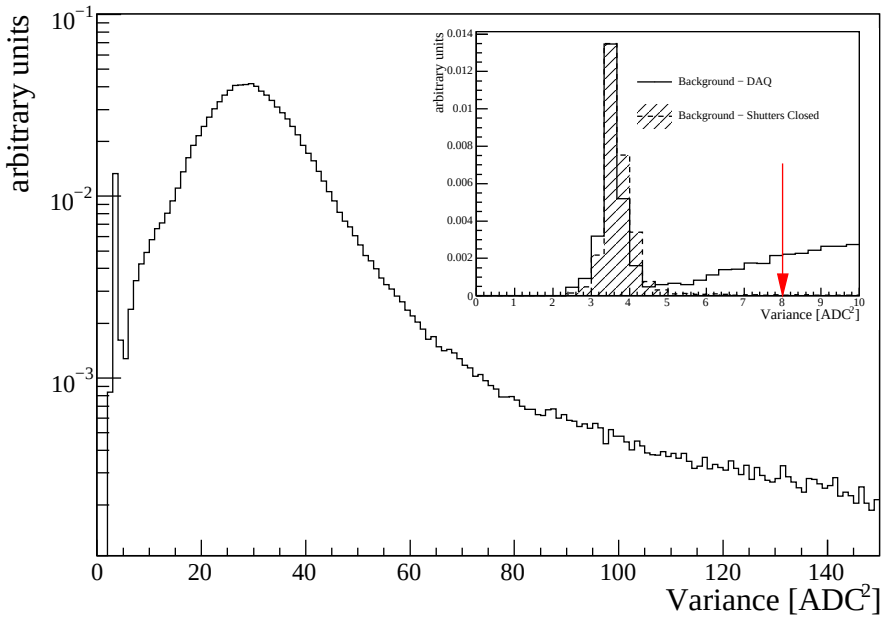

Fig. 2. Distribution of background variances. The main contribution to this background noise is the night-sky background light coming from stars and the direct and scattered moonlight. The upper-right panel shows a magnified view of the low variance region superimposed on data recorded with closed shutters (shaded histogram). The arrow shows the variance threshold used to select good data.

$$\varepsilon_{\mathrm{shutter}} = \frac{T_{\mathrm{open}}}{T_{\mathrm{bin}}} \tag{4}$$

where T_{open} denotes the time (for a given telescope) for which the mean variance over the whole camera is larger than 8 ADC^2 . If background data are not available, no efficiency is calculated. The status flag δ_{tel} is then set to 0.

The deadtime due to the finite readout speed of the DAQ system must also be taken into account. The deadtime is stored on an event-by-event basis in the output of the FD data acquisition. For each telescope, this deadtime $T_{\mathrm{DAQ}}^{\mathrm{dead}}$ is converted into an efficiency of detecting cosmic ray data in the given time interval by:

$$\varepsilon_{\mathrm{DAQ}} = 1 - \frac{T_{\mathrm{DAQ}}^{\mathrm{dead}}}{T_{\mathrm{DAQ}}} \tag{5}$$

where T_{DAQ} is the total running time of the DAQ in the given time interval.

4.2 FD-site dependent sources

Currently two possible sources of inefficiency are known to affect the data taking at the FD-site level.

The first is due to the atmospheric monitoring system. An FD veto is set by the Lidar system before performing laser shots in the field of view of a fluorescence detector. The cumulative Lidar veto time is stored on an event-by-event basis in the data files. This deadtime $T^{\rm dead}_{\rm Lidar}$ is converted into an efficiency by:

$$\varepsilon_{\rm Lidar} = 1 - \frac{T^{\rm dead}_{\rm Lidar}}{T_{\rm DAQ}} \tag{6}$$

This efficiency can be interpreted as the probability of a cosmic ray event falling outside the Lidar vetoed period.

To extend the hybrid detection capability below the SD trigger threshold [4,16], all the FD triggers are sent to and processed by the central data acquisition system (CDAS). It reads out the portion of the surface array closest to the relevant fluorescence building. Then FD and SD data streams are merged to form hybrid events. A source of inefficiency comes from the protection algorithm implemented in the CDAS to prevent the acquisition of long periods of excessive event rates [3]. This veto mechanism induces the loss of hybrid events. An estimate of the event loss probability in a given time interval is calculated by comparing events from the FD data files and from the final merged hybrid files (which only include those sent to CDAS). This recovery mechanism is energy dependent as it is related to the SD trigger probability [17] and is accounted for on an average basis. $\langle \varepsilon_{\rm T3veto}(s,t) \rangle$ is the resulting average efficiency for each FD site s and time t.

4.3 CDAS status

CDAS inefficiencies must also be taken into account. The surface detector array is constantly monitored and a very detailed description of the array status is available with a time resolution of 1 second. In addition to the usually very localized problems of single SD stations, time periods with trigger related problems [4] are excluded in the hybrid on-time via the CDAS status flag

[3] Lightning and other noise events may cause higher FD trigger rates which would cause significant deadtime for the surface array due to the finite readout time of the array.

$\delta_{\rm CDAS}$. Given a constant rate of hybrid events λ, the probability P that the time interval between two consecutive hybrid events is larger than T is given by $P(T) = e^{-\lambda T}$. Taking $\lambda \approx 1.7 \times 10^{-2}$ Hz (1 event per minute) and $T = 600$ sec, then $P = 3.7 \times 10^{-5}$. Based on this calculation, an additional check is performed requiring at least one hybrid event per 10 min time interval.

4.4 Results and cross-checks

For each time t in a given time slot of duration $\mathrm{T_{bin}}$, the fraction of operational time $f(i,t)$, for the telescope i belonging to the FD site s, can be written as:

$$\begin{aligned} f(i,t) = & \varepsilon_{\rm shutter}(i,t) \cdot \varepsilon_{\rm DAQ}(i,t) \cdot \delta_{\rm tel}(i,t) \\ & \cdot \varepsilon_{\rm Lidar}(s,t) \cdot \langle \varepsilon_{\rm T3veto}(s,t) \rangle \\ & \cdot \delta_{\rm CDAS}(t) \end{aligned} \tag{7}$$

where the ε's identify the efficiencies due to the different sources and the δ's are status flags ($\delta = [0,1]$). All the expected sources of inefficiencies have been described in detail in the previous sections.

The time evolution of the full hybrid duty-cycle over 3 years during the construction phase of the observatory is shown in figure 3. It shows the on-time fraction, defined as the ratio of the overall on-time to the time duration of each interval. To avoid pile-up effects in the plot, time bins are chosen to coincide with FD data-taking shifts. Data-taking is currently limited to dark periods with moon-fractions smaller than 60% as seen by each individual telescope: this leads to about 16 nights of data taking per moon-cycle. The scheduled data-taking time fraction is also shown in figure 3 (gray line). A seasonal modulation is clearly visible, since higher fractions are observed in the austral winter during which the nights are longer.

Note that the FD-site at Los Morados became operational in May 2005 and that at Loma Amarilla started in March 2007. After the initial phase of commissioning, the mean on-time is about 12% for all FD-sites, which corresponds roughly to about 70% of the scheduled time fraction. This efficiency is primarily due to weather effects with a minor part determined by detector effects.

A validation of the on-time determination and an estimate of its systematic uncertainty has been performed using data from the Central Laser Facility (CLF) [18]. These data are embedded in the standard FD data stream. As CLF laser shots can be observed from all FD-sites, one can calculate the conditional probability of recording the laser signal in a particular site s given at least one other observation in any other site. The expected number of

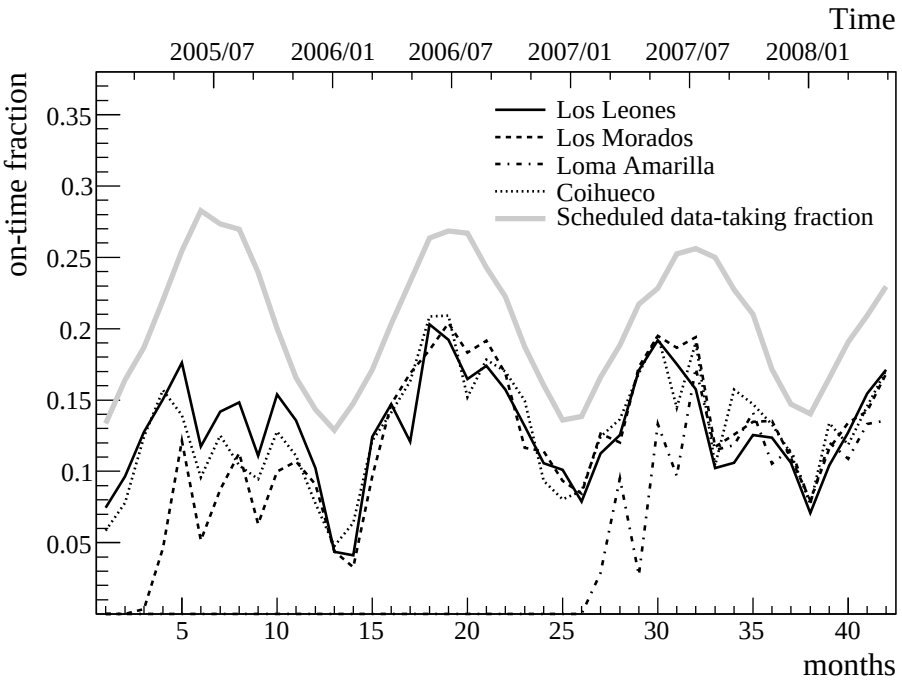

Fig. 3. Time evolution of the average hybrid on-time fraction during the construction phase of the Pierre Auger Observatory. Both the seasonal modulation and the starting of commissioning phases of the different FD-sites are visible. Gray line represents the scheduled data-taking time fraction limited to the nights with moon-fraction lower than 60%.

laser shots in site s can be derived from the on-time of the telescope pointing to the CLF. The laser observation probability is obviously dependent on the transmission coefficient of the atmosphere. The probability of observing a laser during aerosol-free periods, i.e with vertical aerosol optical depth VAOD ≈ 0, is expected to be 100%. A small deviation from this value of about 4% was found and the on-time has been corrected accordingly to account for possibly lost periods.

5 Monte Carlo Simulation

For the calculation of the hybrid exposure, the size of the simulated event sample is crucial for acceptable statistical and systematic uncertainties. For this purpose the simulation activity followed a graded approach with full Monte Carlo analysis for specific studies, like the trigger efficiency, and fast simulations, validated with the full Monte Carlo method, when high statistics were required.

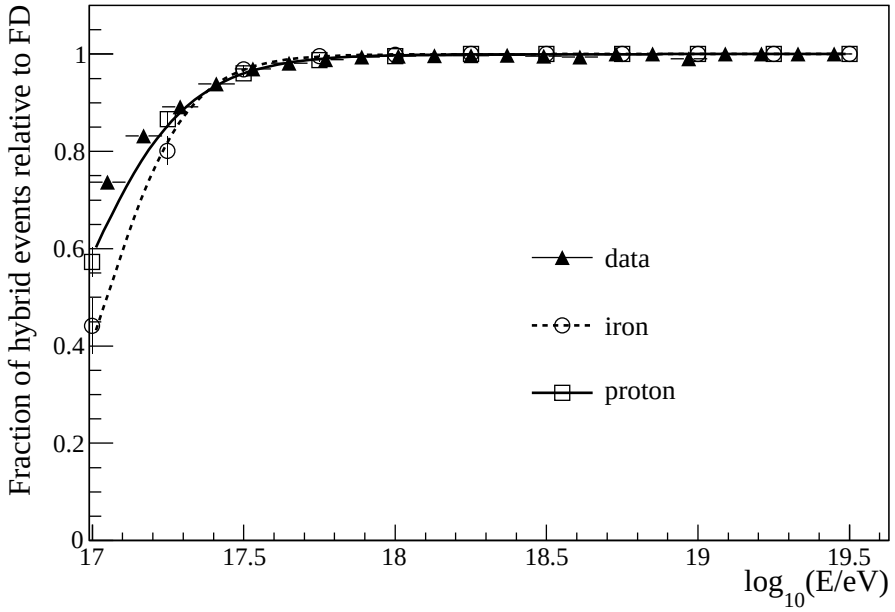

Fig. 4. Relative hybrid trigger efficiency from hybrid simulation for proton and iron primaries. The hybrid trigger efficiency calculated using data is also shown.

5.1 Trigger efficiency

A complete Monte Carlo hybrid simulation has been performed to study the trigger efficiency and the detector performance. The simulation sample consists of about 6000 proton and 3000 iron CORSIKA [19] showers with energies ranging between 10^{17} and $10^{19.5}$ eV. These energies are of particular interest for the trigger studies since they cover both SD and hybrid thresholds. The showers have been generated using respectively QGSJET-II [20,21] and FLUKA[22] as high and low energy hadronic interaction models. The FD simulation chain [23] reproduces in detail all the physical processes involved in the fluorescence technique. It includes the generation of fluorescence and Cherenkov photons in the atmosphere, their propagation through the atmosphere to the telescope aperture, the ray-tracing of photons in the Schmidt optics of the telescopes, and the simulation of the response of the electronics and of the multi-level trigger. The surface detector response is simulated using Geant4 [24] within the framework provided by the Auger Offline software [25]. For this particular purpose we assume the SD array is fully operational and deployed.

In figure 4 it is shown the hybrid trigger efficiency, i.e. the probability of detecting a fluorescence event in coincidence with at least one triggered SD station, is flat and equal to 1 at energies greater than 10^{18} eV, independent of primary mass. The difference between proton and iron primaries increases at lower energies but is negligible at energies as low as $10^{17.5}$ eV. Protons

are slightly more efficient than iron primaries at the lowest energies. This is mainly due to the larger fraction of proton events interacting deeper in the atmosphere. The hybrid trigger efficiency from fluorescence data is also shown in figure 4. Only events landing on an active part of the surface detector have been selected and minimal quality cuts have been applied in order to have a reliable reconstructed energy and to safely derive the trigger probability curve. Data and simulation consistently show that a fluorescence event is always hybrid for energies larger than 10^{18} eV.

In addition, the probability of a shower triggering a given SD station has been studied as a function of primary cosmic ray energy, mass, direction and distance to the shower axis, and a set of "Lateral Trigger Probability" (LTP) functions have been derived and parameterised [26]. For a vertical proton primary shower, each station is on average fully efficient within a distance of 750, 1000, 1300, and 1600 m at energies of $10^{17.5}$ eV, 10^{18} eV, $10^{18.5}$ eV and 10^{19} eV, respectively. Details on this study are discussed in [26].

5.2 Fast simulation

To follow and reproduce the time dependence of the hybrid exposure, each detector configuration must be taken into account. This approach requires a large number of simulations. The method used to achieve this goal within a reasonable computational time relies on the simulation of longitudinal shower profiles generated with CONEX [27], a fast generator based on CORSIKA [19] shower code. After the simulation of the first few ultra-high energy interactions, CONEX switches to numerical solutions of the underlying cascade equations that describe the evolution of the different shower components. Although this method is extremely fast, the most important features provided by full Monte Carlo simulations, including shower to shower fluctuations, are very well reproduced [27,28].

The simulation of the FD response proceeds as in the full method discussed above. Since no ground level particles are generated by CONEX, the SD response cannot be directly simulated. In this case the SD trigger is reproduced using the LTP parameterisation functions. The actual status of the SD array is retrieved using the time of each simulated event. The event trigger probability is then calculated as the convolution of all the LTPs of the working SD stations. This is particularly important for low energy and inclined events.

The SD timing information needed in the hybrid reconstruction mode is provided by a simplified simulation (i.e. SdSimpleSim) implemented in the Offline simulation framework. With this approach the lateral distribution of the air shower is assumed to follow a NKG-like functional form [29,30]. A model gen-

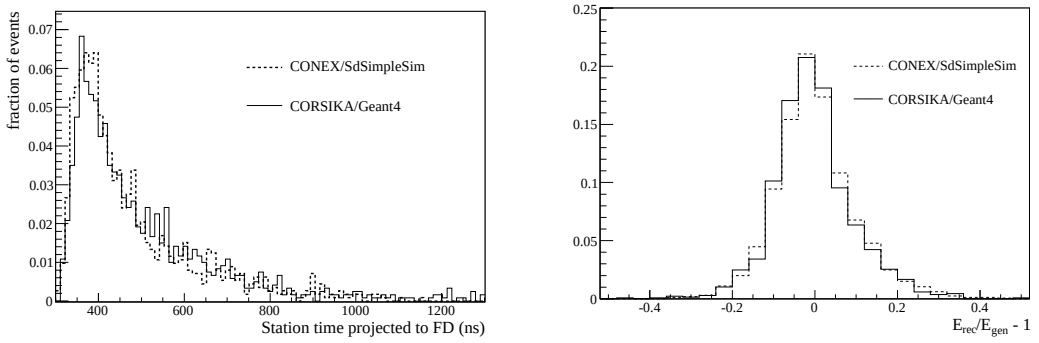

(a) (b)

Fig. 5. Comparison between CORSIKA/Geant4 simulations and the fast CONEX/SdSimpleSim approach. (a): distribution of the time at which the SD station is triggered. (b): difference between the simulated and the reconstructed energies using the hybrid technique. The figures refer to events at $\log_{10}(E/eV) = 18.5$.

erating realistic signal timing for the closest station to the shower axis has been derived from a full Monte Carlo using AIRES [31] simulations. The SdSimpleSim code also includes the simulation of noise triggered stations, which could spoil the reconstruction of the event. The noise rate of the surface detector is self-adjusting to yield 20 Hz per station. As a cross-check, the number of noise triggered stations has been derived from data and the obtained distributions have been parameterized.

Dedicated CORSIKA/Geant4 simulations have been carried out to validate the performance of this fast approach against the full Monte Carlo method. Figure 5 shows the distribution of the station trigger times and the difference between simulated and reconstructed energy as obtained with the two simulation modes. The consistency between these results provides a robust validation of the fast approach and makes it possible to produce of huge number of simulated events.

5.3 Time Dependent Detector Simulation

The Monte Carlo simulation for the calculation of the hybrid exposure has been based on the fast simulation approach described above. In fact for covering all the energy ranges and the phase space of the detector configurations with enough statistical power, the number of simulated events is required to be largely oversampled with respect to the available raw data. The simulation has been designed to reproduce the actual sequencing of the detector status with a resolution of 10 min which corresponds to the time bin slot used for the on-time calculation. First a time is randomly chosen within the sidereal time

interval we want to simulate. Then all the relevant status information about each detector is retrieved from the on-time calculations. Based on the on-time fraction during the simulated time bin, only a sub-sample of the events is sent to the detector simulation.

The CONEX showers used for this purpose have been generated from 10^{17} up to 10^{21} eV. QGSJET-II [20,21] and Sibyll [32] have been used as high energy interaction models. Proton and iron particles are taken as cosmic ray primaries.

To account for the growth of the array with time and problems during the SD data-taking, only the active SD stations are considered during simulation.

For the FD time dependent simulations the values of variance, baseline and trigger threshold averaged over 10 min are considered. The available FD absolute calibration data are used to adjust the simulated electronic gains on a pixel by pixel basis. This scales the shower signal with respect to the FADC trace noise and therefore influences the signal-to-noise ratio. In addition, incorrect cabling in some FD cameras is simulated for the instances discovered in the real detector. Data from the atmospheric monitoring system is used to set the hourly aerosol density profile as measured by the CLF [18] and the monthly mean molecular atmosphere as provided by balloon flights [33].

6 Event selection and validation of Monte Carlo simulation

An unbiased measurement of the cosmic ray flux requires an exposure as free as possible from systematics. To this aim only high quality hybrid events are used.

6.1 Quality cuts

In this analysis high quality hybrid events have been selected using the following criteria:

- since we use the Gaisser-Hillas function [12] to evaluate the total calorimetric energy, a successful fit of the longitudinal profile with this function is required. Moreover, the χ^2 per degree of freedom of the fitted profile should be less than 2.5;
- the energy and shower maximum can only be reliably measured if X_{max} is in the field of view (FOV) of the telescopes (covering 1.5° to 30° in elevation). Events for which only the rising or falling edge of the profile is detected are

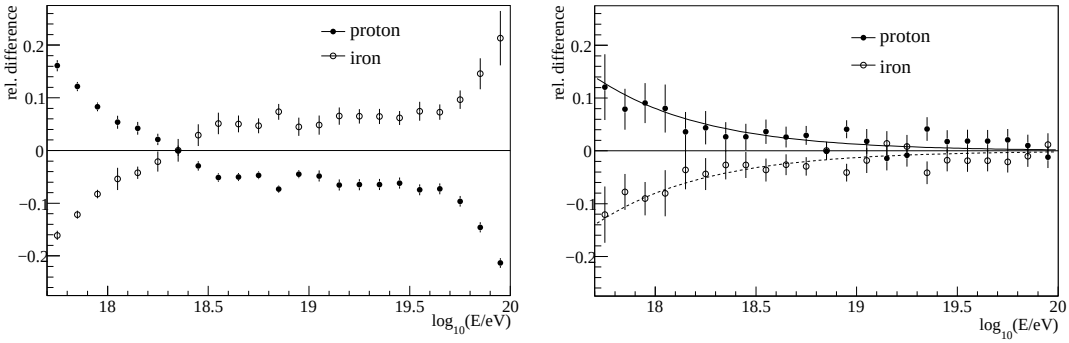

(a) quality selection (b) quality and fiducial volume

Fig. 6. Relative difference between proton and iron exposure with respect to a mean composition exposure, as obtained from the Time Dependent Detector Simulation. In the left panel the dependence on the primary mass is clearly visible. In the right panel this difference is strongly reduced by the fiducial volume cut.

not used, i.e. it is required that the depth of shower maximum be within the minimum and maximum observed depths;

- to avoid potential systematic uncertainties related to the calculation of the Cherenkov light contribution, events with a relative amount of reconstructed Cherenkov light exceeding 50% of the total received light are not used in this analysis;
- a good energy resolution is assured by accepting only events for which the total uncertainty of the reconstructed energy (including the propagated statistical uncertainties of the detected photons, the geometry and the atmosphere) is smaller than 20%.

Furthermore it is required that:

- the aerosol content of the atmosphere is measured [18,34] for the time period of the event to allow a precise calculation of the transmission and scattering of photons in the atmosphere;
- the cloud coverage according to Lidar measurements [34] is lower than 25% at the time of the event, since clouds could obscure part of the longitudinal profile and lead to an event selection inefficiency not accounted for in the aperture simulation.

6.2 Fiducial cuts

In addition to the above mentioned quality criteria, fiducial cuts have been applied to assure a robust calculation of the exposure, independent of the trigger threshold, mass composition and energy scale uncertainty.

To ensure that the probability of a trigger from at least one surface detector station is unity regardless of the primary particle, it is required that

- the energy of the shower is larger than 10^{18} eV;
- the zenith angle of the shower is less than 60°;
- the position of the station used for the hybrid reconstruction is within 1500 m of the shower axis.

The limited field of view of the fluorescence detector and the requirement of observing the shower maximum may both introduce a different selection efficiency for different primary masses. For instance, protons develop deeper into the atmosphere and have a deeper shower maximum than heavy primaries, on average. For vertical events the fraction of events with their maxima falling below the observation level is thus larger for proton primaries and correspondingly the selection efficiency is smaller. The mass dependence of the exposure for showers selected only by quality cuts is clearly visible in figure 6a. At low energies, where events are only detected close to the detector, iron primaries have a smaller exposure because of their shallower $X_{\max}$ that tends to be more often above the upper limit of the FD field of view than it is for protons. At high energies the majority of the showers are far away from the telescopes and the bias is dominated by the lower field of view boundary that disfavors the selection of primary protons.

In order to achieve an almost equal detection probability for all possible primaries, the following fiducial *field of view* cut has been designed:

$$X_{\mathrm{up}}\ [\mathrm{g/cm^2}] \geq 900 + 6 \cdot (\varepsilon - 18) \tag{8}$$

$$X_{\mathrm{low}}\ [\mathrm{g/cm^2}] \leq \begin{cases} 550 - 61 \cdot (\varepsilon - 19.06)^2 & \text{for} \quad \varepsilon < 19.06 \\ 550 & \text{for} \quad \varepsilon \geq 19.06 \end{cases} \tag{9}$$

where $\varepsilon = \log_{10}(E/\,\mathrm{eV})$, and $\mathrm{X_{up}}$ and $\mathrm{X_{low}}$ are the upper and lower boundaries of the telescope field of view which depend on the shower geometry. The application of this cut reduces the primary mass dependence above 10^{18} eV. This is shown in figure 6b.

A further cut was introduced in order to remove the FD trigger threshold effects induced by the energy scale uncertainties. The fluorescence detector trigger is in fact fully efficient for short distances between the shower and the detector. At larger distances the trigger probability decreases. A possible systematic shift in the assignment of the shower primary energy, due to the 22% energy scale uncertainty (see tab. 1), may alter the derived trigger threshold and the exposure. To quantify this effect, the energy assignment of the simulated events can be shifted up and down by 22% before applying the selection

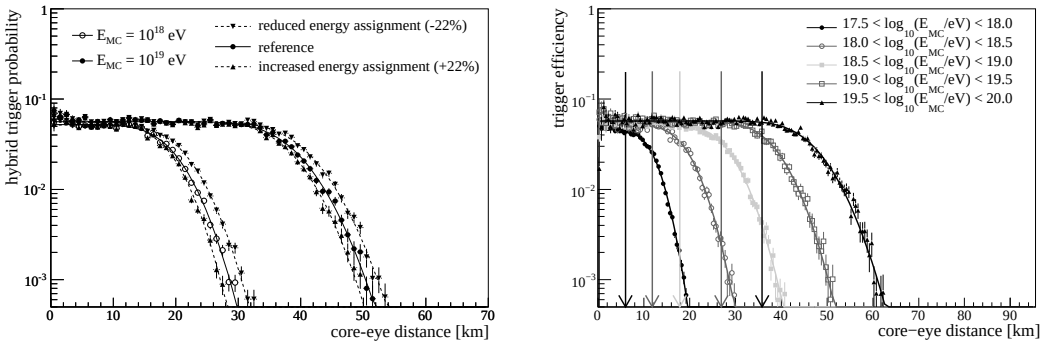

(a) (b)

Fig. 7. The systematic uncertainty of the absolute energy scale of about 22 % would cause significant systematic uncertainties in the fiducial volume and the exposure (left panel). Dedicated event selection criteria are used to remove this dependency (right panel). The arrows show the cut values for the different energies based on eq. (10).

criteria. The effect is shown in figure 7a.

The possible dependence of the trigger threshold on a systematic shift in the energy assignment has been removed by dedicated selection criteria obtained from Monte Carlo studies. The available detection volume is limited by a set of fiducial volume cuts which require the shower core to lie within a distance $D_{\max}$ from the fluorescence detectors:

$$D_{\max}\,[\mathrm{km}] \leq \begin{cases} 24 + 12(\varepsilon - 19) & \text{for} \quad \varepsilon < 18.5 \\ 24 + 12(\varepsilon - 19) + 6(\varepsilon - 18.5) & \text{for} \quad \varepsilon \geq 18.5 \end{cases} \tag{10}$$

As is clearly shown in figure 7b this cut limits the available detection volume to a region in which the fluorescence trigger is saturated even if the energy scale is changed within the known systematic uncertainties ($\pm 22\%$). The exposure calculation thus becomes independent of the trigger threshold and of the absolute energy scale within current estimations of its systematic uncertainty.

6.3 Cross checks

All the above criteria have been applied to both data and MC events. The reliability of the quality criteria are checked by comparing the cut parameter distributions of data and Monte Carlo. Examples of these comparisons, shown in figure 8, indicate a very good agreement between data and Monte Carlo.

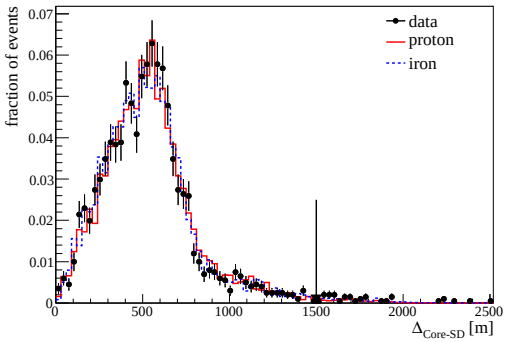

(a) core-station distance

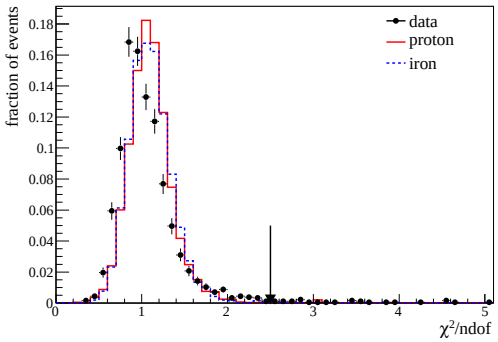

(b) profile $\chi^2/ndof$ for the profile fit

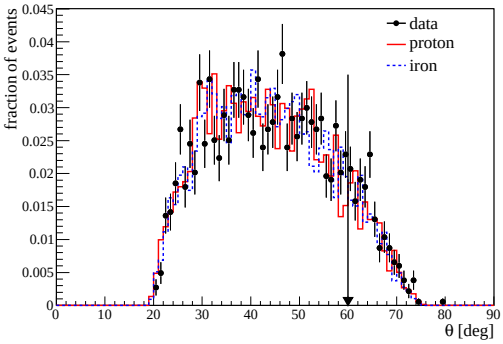

(c) zenith angle

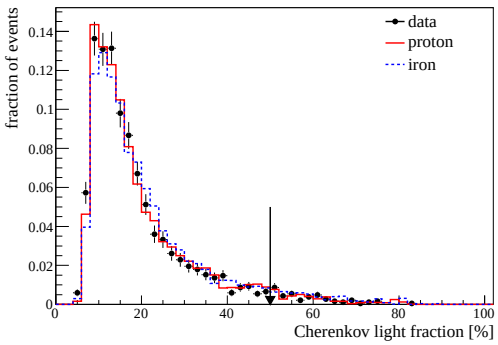

(d) Cherenkov fraction

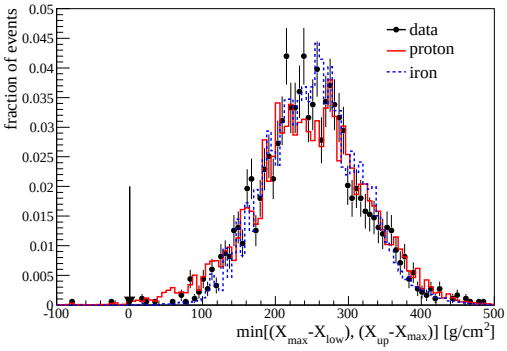

(e) distance of X_{max} to FOV boundary

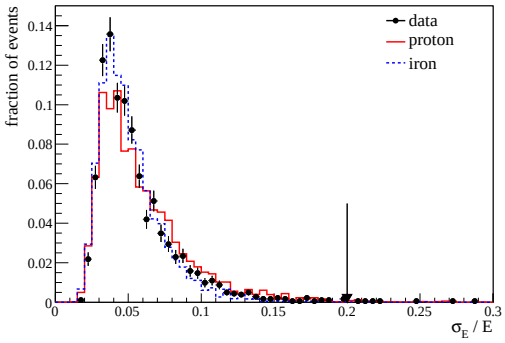

(f) Energy error

Fig. 8. Examples showing the agreement between simulation and data. Proton and iron primaries are shown separately for the simulated data. For each figure all quality and fiducial cuts are applied except the one related to the variable shown. The arrow denotes the selection cut on this variable.

The exposure calculation depends somewhat on the hadronic interaction model used in the Monte Carlo simulation. Different hadronic interaction models predict different fractions of shower energy converted into visible light [13] producing different energy assignments and X_{max} predictions. These differences might affect the selection efficiency and lead to a model dependence in the ex-

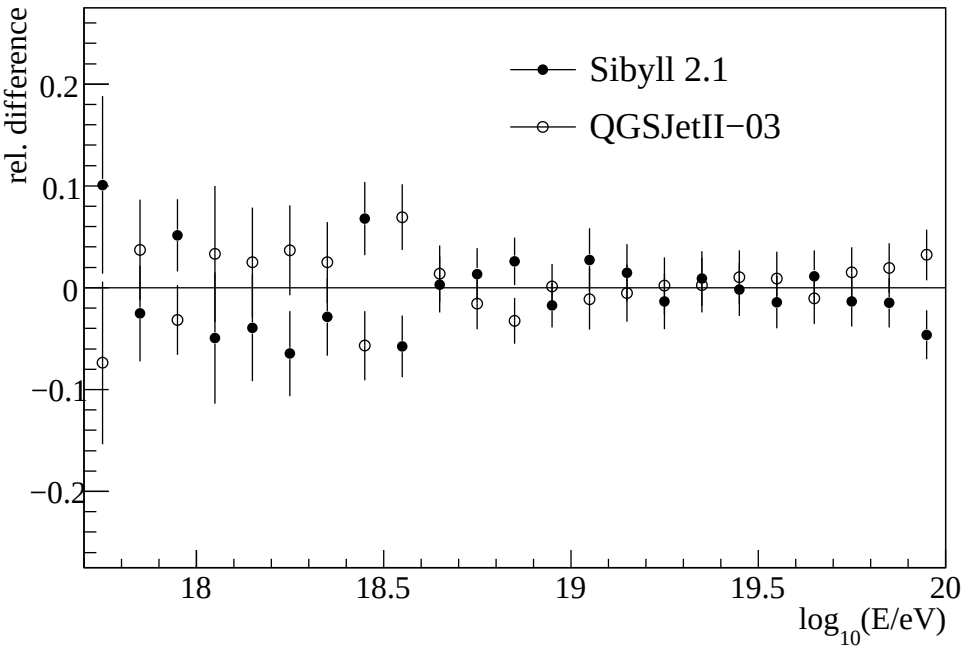

Fig. 9. Relative difference between Sibyll and QGSJetII exposure with respect to the average of the two simulations. All quality and fiducial cuts are applied.

posure. Two models, QGSJetII-03 and Sibyll 2.1 have been used as input for the Time Dependent Detector Simulation and the selection efficiencies have been compared. As is shown in figure 9 the effect is lower than 2% averaged over the whole energy range. For this reason the exposure has been calculated averaging the Monte Carlo samples simulated with the different interaction models.

As mentioned above, the exposure is calculated as a function of reconstructed energy to correct for distortions of the spectrum introduced by the reconstruction of the shower energy. It is well known that this correction depends on the initial assumptions of the true distribution (see eg. [35]), i.e. on the energy distribution of the generated events $N(E)$ in Eq. (3). The exposure has been calculated using different distributions for $N(E)$: power laws with three different spectral indexes ($\gamma = 2,\ 3,\ 3.5$), a broken power law and the combined spectrum measurement from the Pierre Auger Observatory [7]. The ratio of the resulting exposure $\mathcal{E}(E_{\rm rec})$ to the undistorted one, $\mathcal{E}(E_{\rm gen})$, has been calculated for the different cases. From this analysis, the choice of the input spectra used in the Monte Carlo results in a systematic uncertainty lower than 2%.

The availability in the Pierre Auger Observatory of two independent detection techniques allows an overall validation of the Monte Carlo simulation chain with data. As shown in [4] the surface detector trigger is 100% efficient above a few EeV. Since SD data are unaffected by the distance to the FD-site, light attenuation or clouds, the FD trigger and selection efficiency can thus

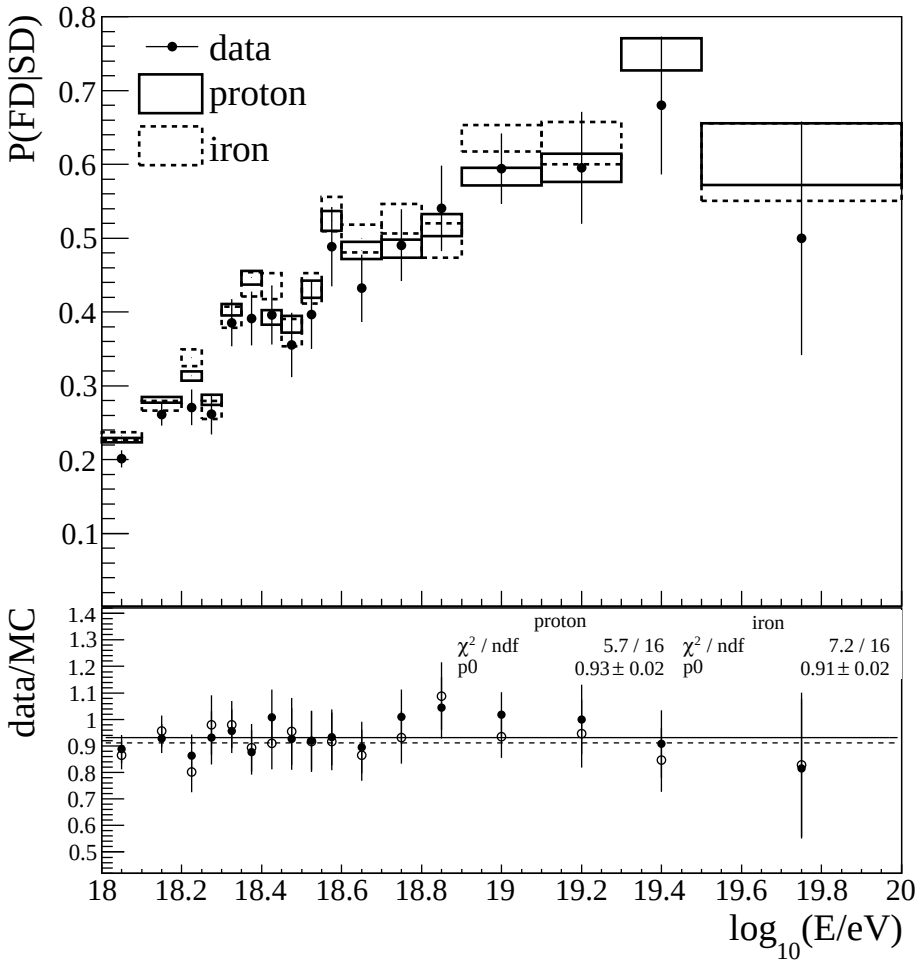

Fig. 10. Conditional probability $P(\mathrm{FD}|\mathrm{SD})$. Comparison between measured and simulated efficiencies. The simulation has been performed using both proton and iron primaries.

be measured directly from the data. A set of high quality SD showers have been selected during the time periods with at least one FD-site taking data. Given this set of N_{SD} showers, we count the number of events that had at least one triggered telescope, $N(\mathrm{FD_{trig}})$, and fulfilled all the selection criteria previously described, $N(\mathrm{FD_{sel}})$. The FD trigger and selection efficiencies can then be estimated from:

$$\varepsilon_{\mathrm{trig}} = P(\mathrm{FD_{trig}}|\mathrm{SD}) = \frac{N(\mathrm{FD_{trig}})}{N_{\mathrm{SD}}} \tag{11}$$

and

$$\varepsilon_{\mathrm{sel}} = P(\mathrm{FD_{sel}}|\mathrm{SD}) = \frac{N(\mathrm{FD_{sel}})}{N_{\mathrm{SD}}}. \tag{12}$$

For each data shower, 20 simulated CONEX showers are generated with the given SD energy for proton and iron primaries. These showers are then pro-

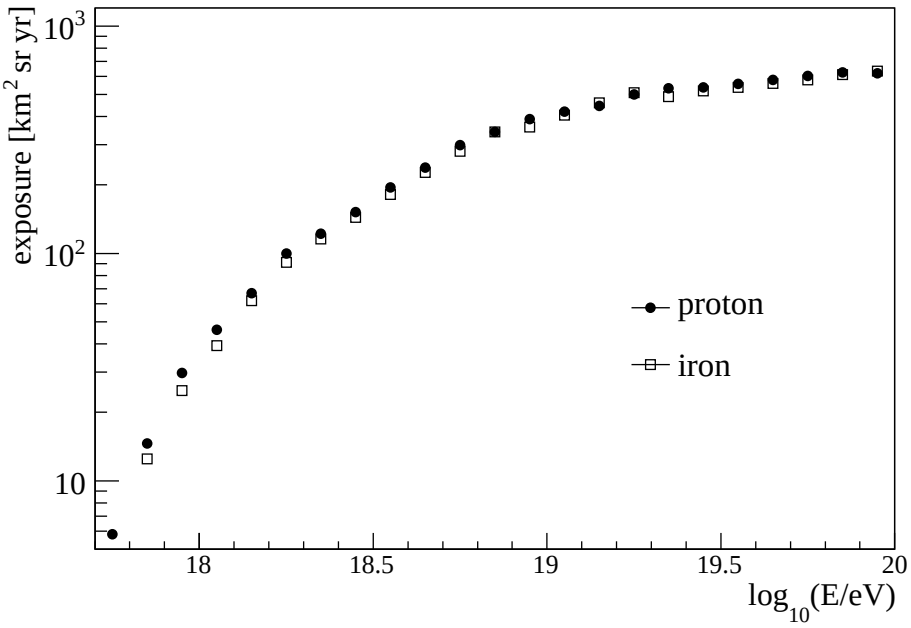

Fig. 11. Hybrid exposure between November 2005 and May 2008 for proton and iron primary particles.

cessed through the Time Dependent Detector Simulation with the same arrival time, direction and core position as measured by the SD, yielding the expected efficiencies:

$$\varepsilon_i^{\mathrm{MC}} = P(\mathrm{FD_i}|\mathrm{gen}) = \frac{N(\mathrm{FD_i})}{N_{\mathrm{gen}}}, \tag{13}$$

where i stands for either the trigger or selection criteria and N_{gen} denotes the number of generated events.

The Monte Carlo prediction is compared with the measurements in figure 10. It can be seen that the shape of the two curves agree for both proton and iron simulations. However we note a normalization factor between simulation and data of 0.92 ± 0.02 assuming a mixed composition of 50% proton and 50% iron nuclei. This could be related to an uncertainty in the on-time, or caused by the poorer energy resolution of the SD.

7 Exposure

The hybrid exposure is shown in figure 11 for both proton (full circles) and iron (open squares) primaries. It is calculated for the data period between

November 2005 and May 2008, and is that used for the hybrid energy spectrum measurement published in [7]. The analysis of the Central Laser Facility shots described in section 4 has revealed a systematic shift in the on-time calculation. To take account of this effect the exposure has been reduced by 4%. Moreover the end-to-end comparison in section 6.3 has shown that the ratio of the true event rate to that expected from Monte Carlo is 0.92 ± 0.02. The systematic uncertainty of this comparison has been estimated to be $\pm$ 5%. Consequently the exposure has been reduced by half of the corresponding correction ($\sim$ 4%) to cover the full range of expectations. These two corrections are included in the exposure shown in figure 11.

A mixed composition of 50 % proton and 50 % iron nuclei has been assumed in the exposure calculation [7]. Numerical values of the hybrid exposure can be found in [36]. The remaining composition dependence has been included in the systematic uncertainty. This was found to be about 8% at 10^{18} eV decreasing down to 1% above 10^{19} eV (figure 6b). The dependence of the exposure on the hadronic interaction model has been studied in section 6.3. The effect is smaller than 2% over the entire energy range used for the calculation of the exposure. The dependence of the exposure on the different input spectra used in the Monte Carlo simulation has also been investigated and found to be smaller than 2%. The overall systematic uncertainty on our knowledge of the hybrid exposure has been obtained by summing all these contributions in quadrature. It ranges from about 10% at 10^{18} eV to 6% above 10^{19} eV.

In figure 12, the growth of the hybrid exposure as a function of time is shown for three different energies. The increase with time shown at each energy comes as a result of the concurrence of different effects, i.e the accumulation of data taking with time and the growth of the SD array. One can also observe faster changes corresponding to the longer FD data-taking periods in the austral winter. The effect due to the growth of the SD array is more marked at higher energies where a larger hybrid detection volume is accessible with the new SD stations.

8 Summary

A method for the calculation of the hybrid exposure of the Pierre Auger Observatory has been developed. The method is mainly based on the Time Dependent Monte Carlo simulation technique. This technique allows the simulation of a sample of events that reproduces in detail the exact configuration of the experimental data taking, including both instrumental and atmospheric conditions.

With this aim the on-time of the hybrid detector has been calculated in a

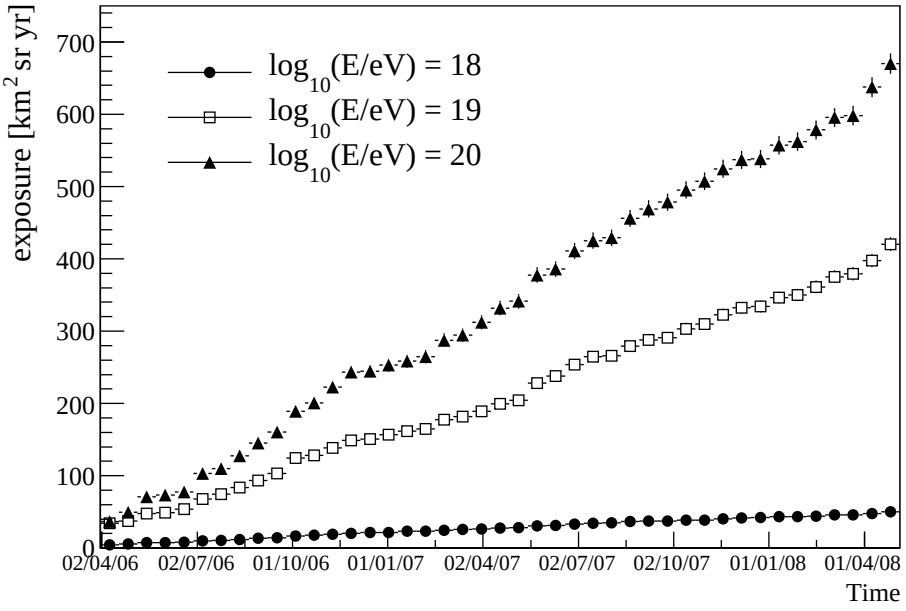

Fig. 12. The growth of the hybrid exposure as a function of time starting from April 2006 up to May 2008 for three different energies.

very accurate way taking into account environmental and instrumental effects occurring at different levels of the DAQ process, with respect to both the FD and the SD. The on-time information has then been used as input for the Time Dependent Monte Carlo simulation.

In order to follow the fast changes of the detector configuration and to get acceptable statistical and systematic uncertainties, a simulation with very high statistics is crucial. A fast simulation has been used, using CONEX shower profiles for the FD simulation and an efficient simulation of the SD response. This fast approach has been validated using a dedicated CORSIKA plus Geant4 simulation. No significant difference has been found between the two approaches.

To obtain an unbiased measurement of the cosmic ray flux the exposure estimate must be as free as possible of systematics. For this reason only very high quality events have been used [7]. To satisfy this aim a set of quality criteria has been developed and discussed in the paper. The effect of the quality criteria has been cross-checked by comparing the data and Monte Carlo distributions; a very good agreement has been found.

The systematic uncertainties arising from the unknown details of mass composition, hadronic interaction physics and the true energy spectrum have been calculated, and residual systematics from the on-time calculation have been estimated. The overall systematic uncertainty on the calculation of the hybrid

exposure has been found to be lower than 10% (6%) at 10^{18} eV (above 10^{19} eV).

9 Acknowledgements

The successful installation and commissioning of the Pierre Auger Observatory would not have been possible without the strong commitment and effort from the technical and administrative staff in Malargüe.

We are very grateful to the following agencies and organizations for financial support: Comisión Nacional de Energía Atómica, Fundación Antorchas, Gobierno De La Provincia de Mendoza, Municipalidad de Malargüe, NDM Holdings and Valle Las Leñas, in gratitude for their continuing cooperation over land access, Argentina; the Australian Research Council; Conselho Nacional de Desenvolvimento Científico e Tecnológico (CNPq), Financiadora de Estudos e Projetos (FINEP), Fundação de Amparo à Pesquisa do Estado de Rio de Janeiro (FAPERJ), Fundação de Amparo à Pesquisa do Estado de São Paulo (FAPESP), Ministério de Ciência e Tecnologia (MCT), Brazil; AVCR AV0Z10100502 and AV0Z10100522, GAAV KJB300100801 and KJB100100904, MSMT-CR LA08016, LC527, 1M06002, and MSM0021620859, Czech Republic; Centre de Calcul IN2P3/CNRS, Centre National de la Recherche Scientifique (CNRS), Conseil Régional Ile-de-France, Département Physique Nucléaire et Corpusculaire (PNC-IN2P3/CNRS), Département Sciences de l'Univers (SDU-INSU/CNRS), France; Bundesministerium für Bildung und Forschung (BMBF), Deutsche Forschungsgemeinschaft (DFG), Finanzministerium Baden-Württemberg, Helmholtz-Gemeinschaft Deutscher Forschungszentren (HGF), Ministerium für Wissenschaft und Forschung, Nordrhein-Westfalen, Ministerium für Wissenschaft, Forschung und Kunst, Baden-Württemberg, Germany; Istituto Nazionale di Fisica Nucleare (INFN), Istituto Nazionale di Astrofisica (INAF), Ministero dell'Istruzione, dell'Università e della Ricerca (MIUR), Italy; Consejo Nacional de Ciencia y Tecnología (CONACYT), Mexico; Ministerie van Onderwijs, Cultuur en Wetenschap, Nederlandse Organisatie voor Wetenschappelijk Onderzoek (NWO), Stichting voor Fundamenteel Onderzoek der Materie (FOM), Netherlands; Ministry of Science and Higher Education, Grant Nos. 1 P03 D 014 30 and N N202 207238, Poland; Fundação para a Ciência e a Tecnologia, Portugal; Ministry for Higher Education, Science, and Technology, Slovenian Research Agency, Slovenia; Comunidad de Madrid, Consejería de Educación de la Comunidad de Castilla La Mancha, FEDER funds, Ministerio de Ciencia e Innovación and Consolider-Ingenio 2010 (CPAN), Generalitat Valenciana, Junta de Andalucía, Xunta de Galicia, Spain; Science and Technology Facilities Council, United Kingdom; Department of Energy, Contract Nos. DE-AC02-07CH11359, DE-FR02-04ER41300, National Science Foundation, Grant No. 0450696, The Grainger Foundation USA; ALFA-EC / HELEN, European Union 6th Framework Program, Grant

No. MEIF-CT-2005-025057, European Union 7th Framework Program, Grant No. PIEF-GA-2008-220240, and UNESCO.

References

[1] J. Abraham et al. (The Pierre Auger Collaboration), "Properties and performance of the prototype instrument for the Pierre Auger Observatory," Nucl. Instr. Meth., vol. 523, no. 1-2, pp. 50–95, 2004.

[2] I. Allekotte et al., "The Surface Detector System of the Pierre Auger Observatory," Nucl. Instrum. Meth., vol. A586, p. 409, 2008.

[3] J. Abraham et al. (The Pierre Auger Collaboration), "The Fluorescence Detector of the Pierre Auger Observatory," submitted to Nucl. Instrum. Meth. A, 2009. arXiv:0907.4282 [astro-ph].

[4] J. Abraham et al. (The Pierre Auger Collaboration), "Trigger and Aperture of the Surface Detector Array of the Pierre Auger Observatory," Nucl. Instrum. Meth. A, vol. A613, pp. 29–39, 2010. arXiv:0907.4282 [astro-ph].

[5] B. Dawson for the Pierre Auger Collaboration, "Hybrid Performance of the Pierre Auger Observatory," ICRC 2007, Merida, arXiv:0706.1105 [astro-ph], 2007.

[6] C. Di Giulio for the Pierre Auger Collaboration, "Energy calibration of data recorded with the surface detectors of the Pierre Auger Observatory," Proc. 31th Int. Cosmic Ray Conf. (Lodz, Poland)(2009) and 0906.2189 [astro-ph].

[7] J. Abraham et al. (The Pierre Auger Collaboration), "Measurement of the energy spectrum of cosmic rays above 10^{18} eV using the Pierre Auger Observatory," Physics Letters B, vol. 685, pp. 239–246, 2010.

[8] J. Abraham et al. (The Pierre Auger Collaboration), "Observation of the Suppression of the Flux of Cosmic Rays above 4 10^{19} eV," Phys. Rev. Lett., vol. 101, p. 061101, 2008.

[9] C. Bonifazi for the Pierre Auger Collaboration, "The angular resolution of the Pierre Auger Observatory," Nucl. Phys. Proc. Suppl., vol. 190, pp. 20–25, 2009.

[10] M. Mostafà et al., "Hybrid Activities of the Pierre Auger Observatory," Nucl.Phys.Proc.Suppl., vol. 165, p. 50, 2007.

[11] M. Unger, B. R. Dawson, R. Engel, F. Schussler, and R. Ulrich, "Reconstruction of Longitudinal Profiles of Ultra-High Energy Cosmic Ray Showers from Fluorescence and Cherenkov Light Measurements," Nucl. Instrum. Meth., vol. A588, pp. 433–441, 2008.

[12] T. Gaisser and A. Hillas Proc. 15th ICRC, vol. 8, p. 353, 1977.

[13] H. M. J. Barbosa, F. Catalani, J. A. Chinellato, and C. Dobrigkeit, "Indirect determination of the missing energy content in extensive air showers," Astropart. Phys., vol. 22, pp. 159–166, 2004.

[14] N. N. Kalmykov, "On application of logarithmic normal distribution to the analysis of experimental data on extensive air showers," Yad. Fiz., vol. 10, pp. 121–129, 1969.

[15] W. Carvalho, Jr., I. F. M. Albuquerque, and V. de Souza, "Effects of the energy error distribution of fluorescence telescopes on the UHECR energy spectrum," Astropart. Phys., vol. 28, pp. 89–97, 2007.

[16] J. Abraham et al. (The Pierre Auger Collaboration), "Observation of the suppression of the flux of cosmic rays above 4 $\times 10^{19}$ eV," Physical Review Letters, vol. 101, p. 061101, 2008.

[17] E. Parizot et. al. for the Pierre Auger Collaboration, "Aperture calculation of the Pierre Auger Observatory surface detector," 29th Int. Cosmic Ray Conf., 2005. astro-ph/0511104.

[18] B. Fick et al., "The Central Laser Facility at the Pierre Auger Observatory," Journal of Instrumentation (JINST), vol. 1, p. 11003, 2006.

[19] D. Heck et al. Forschungszentrum Karlsruhe FZKA-6019, 1998.

[20] N. Kalmykov et al., "Quark-gluon-string model and EAS simulation problems at ultra-high energies," Nucl. Phys. B (Proc. Suppl.), vol. 53, pp. 17–28, 1997.

[21] S. Ostapchenko, "QGSJET-II: Results for extensive air showers," Nucl. Phys. B (Proc. Suppl.), vol. 151, p. 143, 2006.

[22] A. Fassò et al., "FLUKA: a multi-particle transport code," CERN-2005-10, INFN/TC_05/11, SLAC-R-773, 2006.

[23] L. Prado et al., "Simulation of the fluorescence detector of the Pierre Auger Observatory," Nucl. Instrum. Meth., vol. A545, p. 632, 2005.

[24] S. Agostinelli et al. , "GEANT4 - a simulation toolkit," Nucl. Instr. and Meth. A, vol. 506, p. 250, 2003.

[25] S. Argirò et al., "The Offline Software Framework of the Pierre Auger Observatory," Nucl. Instr. and Meth. A, vol. 580, 2007.

[26] Pierre Auger Collaboration, "Paper in preparation,"

[27] T. Bergmann et al., "One-dimensional hybrid approach to extensive air shower simulation," Astropart. Phys., vol. 26, pp. 420–432, 2007.

[28] T. Pierog et al., "Latest Results from the Air Shower Simulation Programs CORSIKA and CONEX," Proc. 30th Int. Cosmic Ray Conf., 2007.

[29] K. Kamata and J. Nishimura, "The Lateral and the Angular Structure Functions of Electron Showers," Prog. Theoret. Phys. Suppl., vol. 6, p. 93, 1958.

[30] K. Greisen Prog. Cosmic Rays Phys., vol. III, p. 26, 1965.

[31] S. Sciutto et al., "AIRES, a system for air shower simulation," http://www.fisica.unlp.edu.ar/auger/aires.

[32] E.-J. Ahn, R. Engel, T. K. Gaisser, P. Lipari, and T. Stanev, "Cosmic ray interaction event generator SIBYLL 2.1," Phys. Rev. D, vol. 80, p. 094003, 2009.

[33] J. Abraham et al. (The Pierre Auger Collaboration), "A Study of the Effect of Molecular and Aerosol Conditions in the Atmosphere on Air Fluorescence Measurements at the Pierre Auger Observatory," Astropart. Phys., vol. 33, p. 108, 2010. arXiv:1002.0366 [astro-ph].

[34] S. BenZvi et al., "The Lidar system of the Pierre Auger Observatory," Nuclear Instr. and Meth., vol. A574, p. 171, 2007.

[35] G. Cowan, Statistical Data Analysis. Oxford Science Publications, 1998.

[36] P. A. Collaboration, "Hybrid Exposure of the Pierre Auger Observatory," http://www.auger.org/technical_info/exposure/hybrid_exposure.txt.